Propagation of modulated electron and X-ray beams through matter and interactions with radio-frequency structures

J. R. Harris, and R. B. Miller

Articles you may be interested in

Particle-in-cell modeling of the nanosecond field emission driven discharge in pressurized hydrogen
Journal of Applied Physics **123**, 083303 (2018); 10.1063/1.5021129

Analysis of localized surface plasmon resonances in gold nanoparticles surrounded by copper oxides
Journal of Applied Physics **123**, 083103 (2018); 10.1063/1.5021402

Effect of electrode configuration on the uniformity of atmospheric pressure surface dielectric barrier air micro-discharge
Journal of Applied Physics **123**, 083301 (2018); 10.1063/1.5012912

High performance of visible-NIR broad spectral photocurrent application of monodisperse PbSe nanocubes decorated on rGO sheets
Journal of Applied Physics **123**, 083102 (2018); 10.1063/1.5017226

Understanding the adhesion and optical properties of eutectic metal alloys for solution-processed electronics
Journal of Applied Physics **123**, 083104 (2018); 10.1063/1.5011464

Engineering electric and magnetic dipole coupling in arrays of dielectric nanoparticles
Journal of Applied Physics **123**, 083101 (2018); 10.1063/1.5018312

CrossMark
← click for updates

Propagation of modulated electron and X-ray beams through matter and interactions with radio-frequency structures

J. R. Harris[1] and R. B. Miller[2]

[1]*Directed Energy Directorate, Air Force Research Laboratory, Albuquerque, New Mexico 87106, USA*
[2]*Verus Research, Albuquerque, New Mexico 87110, USA*

The generation and evolution of modulated particle beams and their interactions with resonant radiofrequency (RF) structures are of fundamental interest for both particle accelerator and vacuum electronic systems. When the constraint of propagation in a vacuum is removed, the evolution of such beams can be greatly affected by interactions with matter including scattering, absorption, generation of atmospheric plasma, and the production of multiple generations of secondary particles. Here, we study the propagation of 21 MeV and 25 MeV electron beams produced in S-band and L-band linear accelerators, and their interaction with resonant RF structures, under a number of combinations of geometry, including transmission through both air and metal. Both resonant and nonresonant interactions were observed, with the resonant interactions indicating that the RF modulation on the electron beam is at least partially preserved as the beam propagates through air and metal. When significant thicknesses of metal are placed upstream of a resonant structure, preventing any primary beam electrons from reaching the structure, RF signals could still be induced in the structures. This indicated that the RF modulation present on the electron beam was also impressed onto the x-rays generated when the primary electrons were stopped in the metal, and that this RF modulation was also present on the secondary electrons generated when the x-rays struck the resonant structures. The nature of these interactions and their sensitivities to changes in system configurations will be discussed. https://doi.org/10.1063/1.5017752

I. INTRODUCTION

The generation, propagation, and use of modulated electron beams have been investigated for various applications since Edison's rediscovery of thermionic emission,[1] and pre-dates the discovery of the electron itself. These modulated beams are at the heart of all vacuum electronic devices, from the earliest diodes[2] to the most modern free-electron lasers[3] and microwave sources,[4] and all charged particle beams feature some degree of modulation, even if that modulation occurs only when the beam is gated on and off. Numerous gating and modulation techniques have been developed,[5–10] and the propagation of modulated electron beams in vacuum has been extensively studied.[11] Even in vacuum, the physics of modulated electron beams is rich and nuanced, particularly in beams where space charge plays an important role. Longitudinal space charge waves can be launched from beam modulation[5] or beam ends,[12] interacting with slow wave,[13] resistive,[11] or magnetic[14] structures. These waves can interfere with each other, altering the beam modulation as stored energy in the beam is converted from potential to kinetic and back.[15] Nonlinear, soliton-like waves can be generated,[16] and nonlinear processes can lead to shock formation, halo generation, and beam heating.[17] Space charge also couples the transverse and longitudinal properties of electron beams,[11] altering a beam's interaction with apertures[18,19] and focusing channels.[20–22]

If the restriction of propagation in a vacuum is removed, a host of additional factors is introduced, including scattering, plasma generation and dissipation, and formation of multiple generations of secondary particles. Extensive work on the transport of electron beams in background gases was conducted in the 1980s, much of which emphasized overcoming the difficulties in transporting very high current, moderate energy, relatively long beams through the atmosphere, where beam modulation was not of primary concern.[23,24] However, some later work did consider the interaction of modulated electron or x-ray beams with electronic systems,[25] and the use of modulated x-ray signals for communication[26–28] and ranging[29] applications is currently under investigation. In such a role, modulated x-rays have the advantages of increased directionality and reduced losses due to intervening materials, such as the plasma formed around a re-entering spacecraft,[30,31] and are therefore of particular interest in spaceflight applications.

The objective of our present work is to investigate the propagation of modulated electron and x-ray beams through matter and their subsequent interactions with radiofrequency (RF) structures. Because RF structures can be made sensitive to specific frequency content in the beam modulation, changes in their response can be used to infer the existence of, or changes in, beam modulation resulting from propagation through matter and the accompanying processes such as scattering, absorption, and secondary particle generation. These investigations were performed through experimental tests of S-band and L-band cavities and waveguides at the Idaho Accelerator Center (IAC), where a pair of RF electron linacs, one S-band and the other L-band, are conveniently co-located. Like all RF linacs, these generate beams modulated at the RF frequency. Additionally, the L-band machine tends to introduce a beam envelope modulation with a

structure on a typical time scale of several hundred nanoseconds. While the machine is generally tuned to suppress this structure, for these tests, it was tuned to enhance it.

In the sections that follow, we will first discuss the experimental apparatus used in this work, including the IAC linacs and our RF test structures. Response of these structures as a function of their orientation and state, and of the distance traveled by the beam through air or metal, will be considered. Changes in this response as the beam electrons are replaced by x-ray photons will also be discussed.

II. EXPERIMENTAL APPARATUS

A. Accelerators

To meet our objectives, it was important to have the ability to generate electron beams with different types of modulation, with that modulation having characteristic frequency content over a wide range but particularly including RF bands that would be convenient for testing. In principle, this could be accomplished in a number of ways, for instance RF modulation of a gridded gun or photomodulation using a laser pulse train.[32] An alternate approach would be to use an RF linac, in which the beam frequency content will include the linac's RF frequency. However, that frequency is tied to the mechanical dimensions of the accelerating structure, and cannot be tuned over a wide range. Additionally, many accelerator facilities standardize on a particular frequency band for both technical and logistical reasons.

However, this is not true of IAC, which is home to an impressive array of accelerators, providing a wide range of energies, currents, and pulse formats.[33] In particular, they have both a 25 MeV S-band electron linac and a 44 MeV L-band electron linac available in the same shield vault, providing a convenient approach to pursuing our goals. While these machines are each capable of producing a range of energies, currents, and pulse formats, we standardized on a single set of parameters for each machine for these tests. The S-band linac (a Varian Clinac) was operated at an RF frequency of 2856.200 MHz, a beam energy of 20.6 MeV, a beam current of 85 mA (measured with a Pearson coil just downstream of the 1 mil Ti foil exit window), and a macropulse length of 4 μs. Our testing location was at the machine's 0° port. The machine exhibited very good shot to shot stability, with little structure present on the Pearson coil signal. The L-band linac was operated at an RF frequency of 1299.9 MHz, a beam energy of 24.75 MeV, a nominal beam current of 140 mA, and a pulse length of 2.2 μs. Beam extraction was taken through a 1 mil Ti window on the machine's 90° port, with the current measured using an in-flange Bergoz Integrating Current Transformer (ICT). The beam extracted from this port naturally exhibits some structure on a characteristic time scale of a few hundred nanoseconds. The machine is normally tuned to suppress this structure, but in our case, it was tuned to enhance that structure in order to provide additional, lower-frequency modulation on the beam. In this configuration, the beam exhibited significantly more shot-to-shot variation than the beam from the S-band machine. As a result, several data points were typically taken at every test configuration (i.e., cavity/waveguide location, orientation, distance, etc.), with the beam current and RF

structure signals recorded at the corresponding locations in their respective, modulated waveforms.

Beam envelopes in air, downstream of the Ti exit windows, are shown in Fig. 1 (IAC is located 1463 m above sea level). These envelopes were measured by exposing a series of glass plates to the beam, which darken when struck by the beam, and then measuring the horizontal and vertical widths. All distances in this paper will be referenced with respect to the location of the exit windows. The S-band linac beam was essentially round, with only a small degree of asymmetrical halo detectable at very short ranges. The L-band beam was ellipsoidal, with a slightly larger horizontal than vertical width, and a skew rotation of about 8°. Due to mechanical constraints in the shield vault, a slightly longer range in air was available with the S-band machine than with the L-band machine.

B. RF structures

To test interactions of modulated beams with RF structures after the beams' passage through air or metal, four test articles were constructed (Fig. 2). Two of these were cylindrical aluminum cavities designed to support modes at S-band and L-band. Each cavity was equipped with a pickup ($\dot{B}$) loop to detect the azimuthal magnetic field in the cavity. Additionally, each cavity was equipped with removable end plates sealed with rubber gaskets, and with Kwik-Flange (KF) type vacuum fittings to allow the cavities to be backfilled with gas or pumped to a weak vacuum; these capabilities were not used during the testing described here. Cavities were tuned by addition of copper tape to the inside circumference of the cylindrical cavity wall. The cavity end plates could be weakly attached or removed entirely to spoil their quality factor (Q), which ranged from about 200 to 238 for the S-band cavity, and was approximately 930 for the L-band cavity (see Appendix). Sensitivity of each cavity to out-of-band signals was low. For example, when the S-band cavity was tested with a network analyzer, the signal at 1.3 GHz was down by 50 dB and the signal at 2.6 GHz was down by 40 dB from the S-band resonance peak when configured in a high-Q state. Similarly, the L-band cavity tuned to 1.3007 GHz showed higher order mode resonances at 2.070, 2.770, 2.980, and 3.101 GHz, which did not include the S-band linac frequency of 2856 MHz or the higher integer harmonics of 1.3 GHz that might be present on the beam. The pickup loop was inserted through the cavity wall and
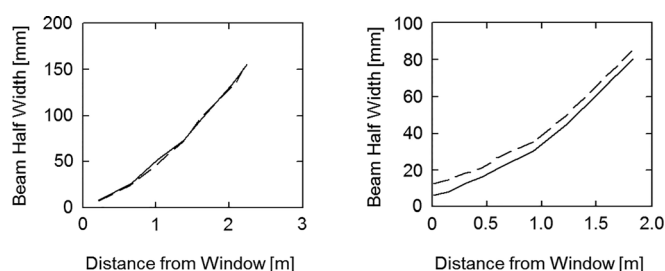

FIG. 1. Beam envelopes from the S-band linac (left) and L-band linac (right) beams at our standard operating points, showing vertical (solid) and horizontal (dashed) half-widths.
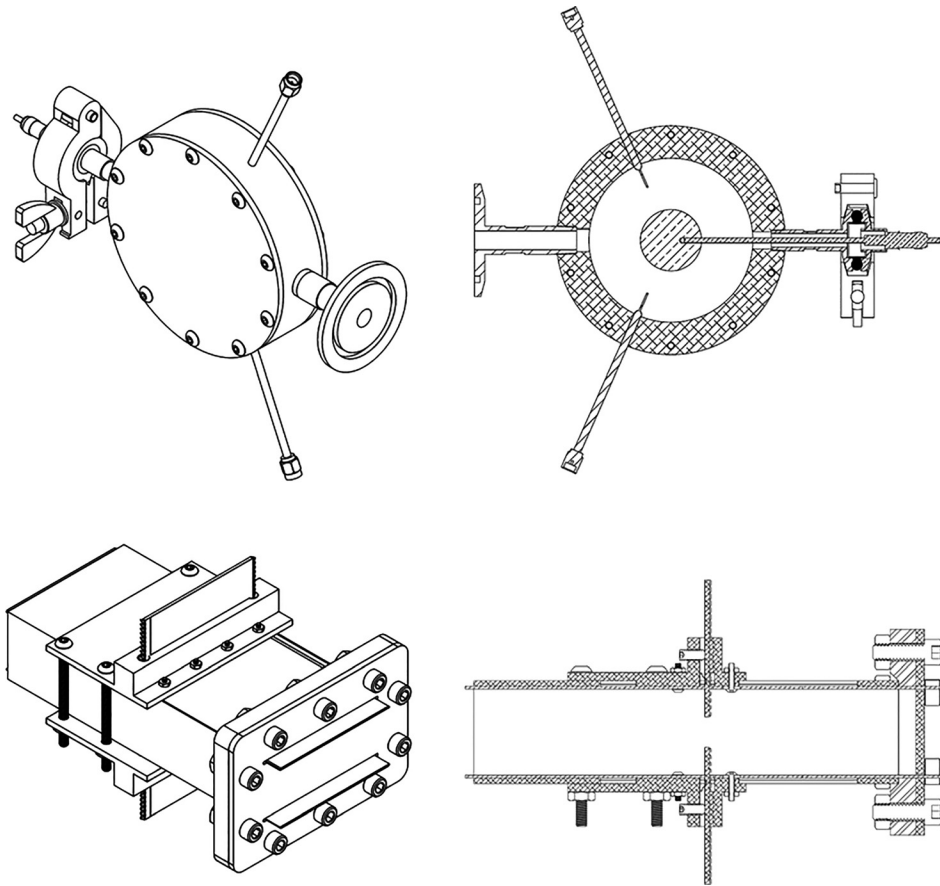
FIG. 2. External and cross-sectional diagrams of the S-band cavity (top) and S-band waveguide variable-geometry interaction region (bottom). Designs for the L-band structures were essentially similar. The S-band cavity diagram shows two antennas, while only a single pickup loop was used in the actual experiment. Also, the cavity is shown with a charge-collection plate installed; this was not used in the tests reported here.

held in place by Torr Seal; this proved a weak point in their design, as the Torr Seal was accidentally broken on the S-band cavity, allowing the coupler to move during handling, changing its coupling efficiency. However, data taken at the same beam parameters, with the cavity in the same location and orientation and with the end plates off, both before and after this change in the coupler position, allow a correction factor to be determined so that all datasets can still be compared against each other. Because the pickup loops themselves were not calibrated, we report signal strength measured at the crystal detector, corrected for added attenuation (Fig. 3), rather than in terms of power or field strength in the cavities themselves.

Two test items were also constructed from WR 650 and WR 284 waveguides, for L-band and S-band respectively. These were further equipped with a variable-opening, variable-location iris, forming a cavity or interaction region at one end of the waveguide. At the other end, the waveguide was connected to a waveguide-to-coax transition.

It is important to emphasize that the waveguide and cavity probe signals are different: with the waveguide we are measuring the microwave power generated in the structure, while the cavity probe is sensitive to both the induced cavity fields and the fields produced by the beam itself. For the cavities and waveguides, the signal detected by the pickup loop or waveguide-to-coax transition was sent through an attenuator (attenuations of 0 dB, 10 dB, and 20 dB were used) to an Agilent 8474B crystal detector and then to a digitizing oscilloscope (Fig. 3).

III. BEAM TRANSPORT THROUGH AIR

A. S-band cavity

To assess the impact of beam modulation on the induced cavity signal at various distances and orientations in air, the S-band cavity was tested with electron beams from both the S-band and L-band linacs, with the cavity tested in both high-Q and low-Q configurations. The use of both linacs allowed the cavity to be exposed to electron beam modulation at two distinct fundamental frequencies, one in-band for the cavity and one out-of-band.

Figure 3 shows the cavity orientations used. The cavities were aligned with the nominal beam center using an alignment laser provided by IAC, which can be directed to counterpropagate along the beam axes on the two linacs, and is aligned with the center of images of the two beams obtained using glass plate exposures as described above. In 0° on-axis and 90° cases, the center of the cavity wall facing away from the beam window was aligned with the laser, while in 0° off-axis cases, the laser was aligned with the edge of the cavity wall, so that approximately half of the laser spot was blocked and half was not blocked. (Note that a different alignment was used for the off-axis tests described in Sec. IV A.)

Cavity locations are measured as the distance between the Ti window and the leading edge of the cavity; note that the distance from the leading edge of the cavity to the cavity center differs slightly in the 0° and 90° cases. Signal is reported as RF power detected at the crystal, in dBm, adjusted for added attenuation, and normalized by the beam current. In
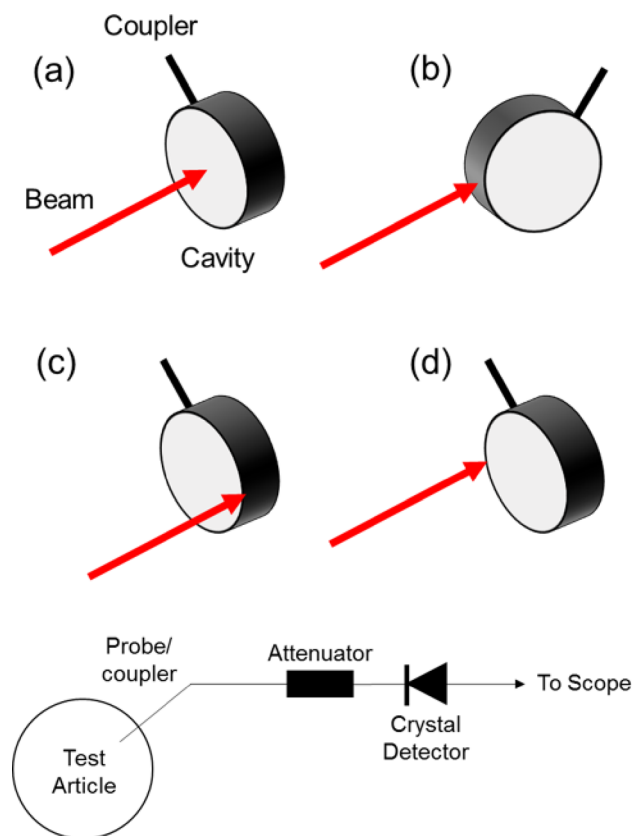
FIG. 3. (Top) Cavity alignment and orientation to the electron beam: (a) 0° orientation, on-axis; (b) 90° orientation; (c) 0° orientation, off-axis away from coupler; (d) 0° orientation, off-axis towards coupler. (Bottom) Measurement setup used on both cavities and waveguides.

the case of the S-band linac, the shot to shot stability was extremely good, and the nominal value of 85 mA is used in all cases, with only a single measurement typically taken at each distance. For the L-band linac, the cavity signal and the beam current were measured at the corresponding locations in the low-frequency envelope modulation, which was clearly present in both the beam current and cavity signals. The data plotted here for the L-band linac represents the average of at least three shots taken at each distance.

The resultant data are shown in Fig. 4. This figure consists of four panels, with the upper row presenting data taken with the S-band linac, the lower row presenting data from the L-band linac, the left column presenting data with the cavity in a low-Q state, and the right column presenting data with the cavity in a high-Q state. In each panel, four curves are shown, labeled (a)–(d). Each of these curves corresponds to a different cavity orientation with respect to the beam, with the letters referring to the orientations, as shown in Fig. 3. In each panel, the horizontal axis is the distance from the cavity leading edge to the beam window, while the vertical axis is the cavity power detected at the crystal, normalized by the corresponding beam current.

It is not particularly surprising that an electron beam modulated at S-band, directed along the axis of a high-Q resonant cavity tuned to the beam modulation frequency, would be effective in driving fields in that cavity. However, these data show that easily detectable signals were produced

in the S-band cavity under a wide range of conditions, and it indicates that the general response of the cavity due to changes in the distance and orientation followed certain trends which were qualitatively similar irrespective of the cavity Q or the fundamental frequency of the linac used. This emphasizes that the resonant drive of cavity modes is not the only interaction at play, although it is the most effective, as indicated by the much stronger signal detected in the optimal, matched frequency, high-Q, on-axis case [Fig. 4, top right panel, trace (a)]. In particular, the 90° data in the S-band cases, and both the on-axis 0° and 90° data in the L-band cases, were very similar irrespective of cavity Q at short distances where differences in beam spreading had not yet come into play, supporting the idea that these signals were primarily produced through non-resonant interactions, such as direct sensing of the beam field by the $\dot{B}$ loop. Indeed, with the cavity end plates removed, and the cavity walls intercepting none of the beam, a strong signal was still detectable simply due to the $\dot{B}$ loop sensing the modulated magnetic field from the electron beam (Fig. 5).

A closer examination of the similarities and differences exhibited by these datasets is now in order. To begin, we note that the 0°, on-axis curves (a) are generally the strongest signals detected in each combination of cavity Q and linac (although in certain cases they are matched by other curves), and that they decrease monotonically with increasing range in air.

The 90° case, whose data are plotted in curves (b), reflects a purely non-resonant interaction and generally has signal strength less than or equal to that of the on-axis case (a), with the difference in the value of these curves corresponding to how far away the tested case is from the ideal resonant drive case. Thus, the largest difference between these curves is for the S-band linac, high-Q case, while the smallest difference between them is for the L-band linac, low-Q case. Additionally, both the 0° on-axis and 90° curves (a) and (b) exhibit a similar monotonic decrease in signal strength as a function of increasing distance.

The off-axis cases (c) and (d) show noticeably lower signal strength than the on-axis and 90° cases under most circumstances. With these off-axis data, some important distinctions begin to emerge between the four testing cases shown in Fig. 4.

For the S-band beam datasets, the off-axis curves show a clear trend, beginning at a low level, increasing to a maximum value at about 1.5 m, and then approaching the signal level detected in the on-axis cases (a). This general trend can be explained by the relatively rapid radial expansion of the electron beam produced by the S-band linac under the accelerator settings used for this test, as shown in Fig. 6. That figure replots the off-axis curves (c) and (d) for both the low-Q and high-Q cases on a single pair of axes. At four locations, we have also indicated the relative size and orientation of the cavity (black circles with center indicated by a cross) and the beam (red circle); the inner and outer black circles indicate the inner and outer surfaces of the cylindrical cavity wall. The beam center is collocated with the cavity edge, which is how the cavity was aligned with respect to the beam axis for these tests, and the vertical and horizontal beam sizes are
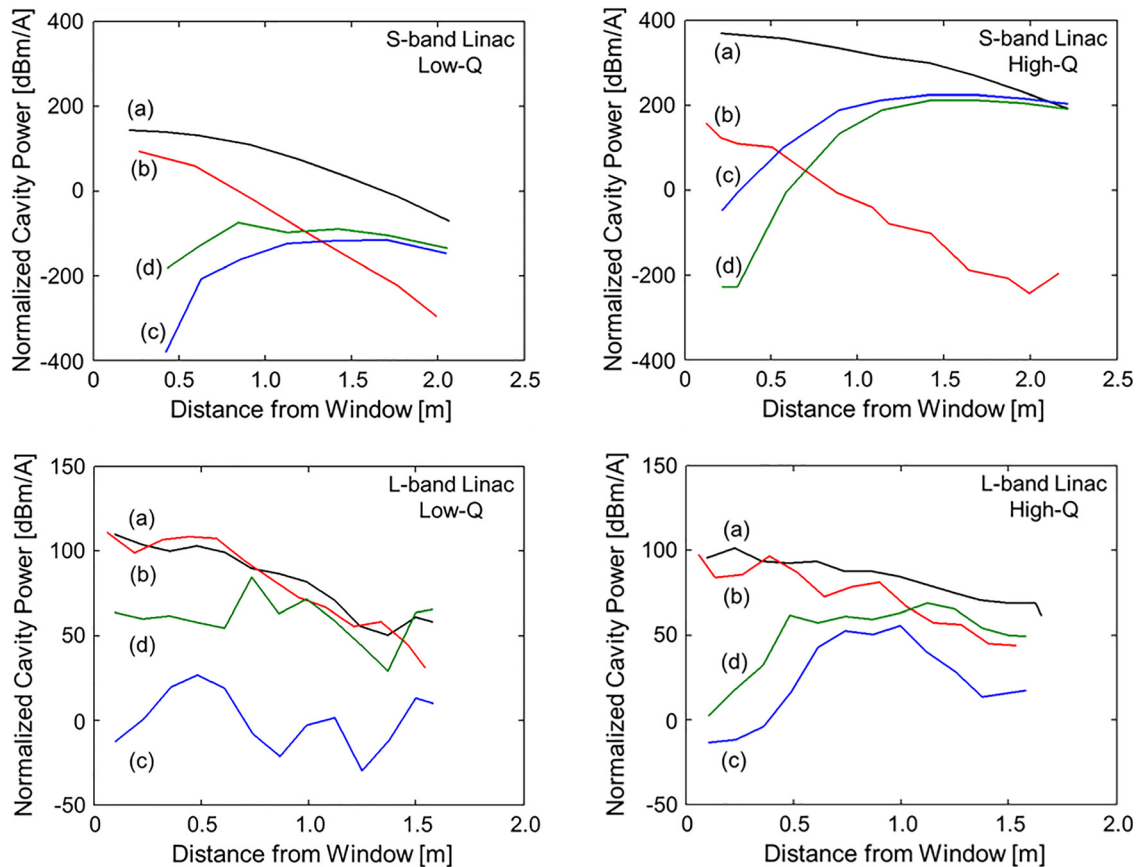
FIG. 4. Cavity power detected at the crystal, normalized by the beam current, as a function of distance from the beam window, for the S-band cavity struck by the electron beams from the S-band (top) and L-band (bottom) linacs, under both low-Q (left) and high-Q (right) conditions. Letters refer to cavity orientations and offsets, as shown in Fig. 3: (a) 0° orientation, on-axis; (b) 90° orientation; (c) 0° orientation, off-axis away from the coupler; and (d) 0° orientation, off-axis towards the coupler. Each point in the S-band graphs represents a single data point, while each point in the L-band graphs is the mean of at least three data points.

from Fig. 1. When the cavity is very close to the beam window, the beam size is small. Very nearly half of its current hits the cavity, but that current is far from the cavity center, where it must be to efficiently drive the cavity fundamental mode. As the cavity is moved farther from the window, the beam size increases. Initially, the fraction of beam current
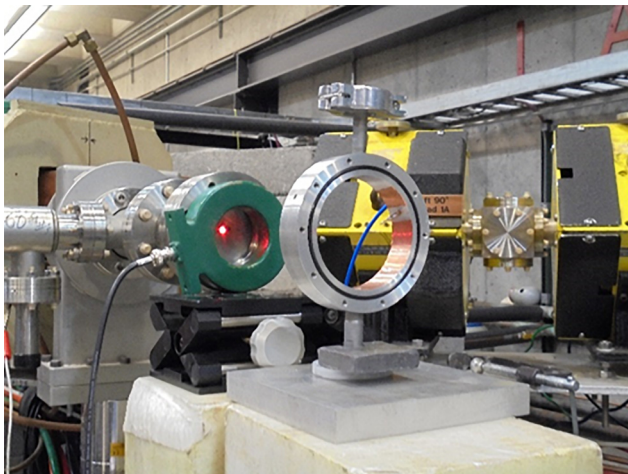

FIG. 5. S-band cavity test with end walls removed. The alignment laser spot is visible on the Ti beam window, as are the green Pearson coil, the cavity KF fittings and gasket, and the copper tape used to tune the cavity resonance.

striking the cavity only falls slowly with increasing distance, and this loss in intercepted beam current is more than compensated for by having an increased amount of current passing through the cavity near its center, where the interaction is increased. The peak in the data traces for both the high-Q and low-Q cases occurs between the distance at which the beam edge has just passed through the cavity center, and the distance at which the beam fills the cavity interior. Note that the beam edge indicated here and in Fig. 1 corresponds roughly to the 20% intensity contour in the glass plate exposures, and therefore the peak current density arriving at the cavity center is not likely to occur until slightly after the beam radius exceeds the cavity radius. The detected power in the low-Q cases is lower, which is reasonable because the lower Q will weaken the effectiveness of the on-axis resonant drive. As the cavity is still moved farther from the beam window, the beam size continues to increase. This reduces the current density in the beam, thereby reducing the current available near the cavity axis to optimally drive the cavity mode. Additionally, an increasing fraction of the beam misses the cavity entirely, also reducing the effectiveness of any non-resonant interactions with the cavity. Accordingly, the detected cavity signals begin to decrease. As the beam radius becomes larger than the cavity radius, the quantity and the location of current intercepted by the cavity depend
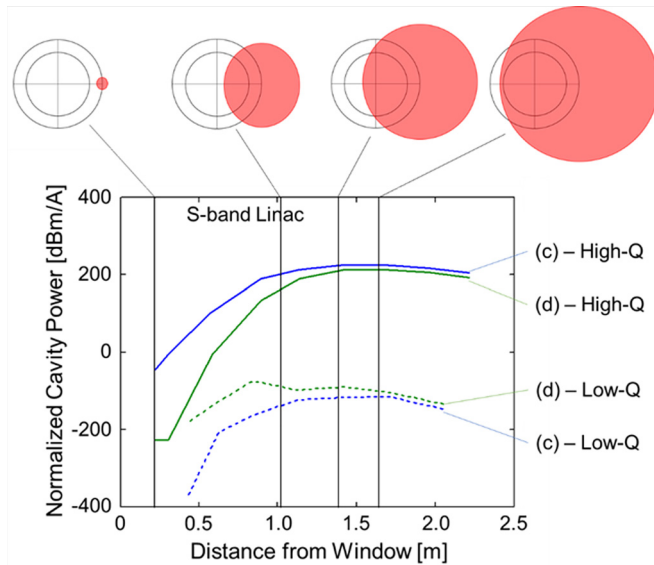
FIG. 6. Dependence of cavity signals on the beam size for the S-band cavity offset from the beam axis on the S-band linac. The green and blue traces are as shown in Fig. 4; for clarity in this figure, the high-Q cavity signals are shown with solid lines, while the low-Q cavity signals are shown with dashed lines. The four images at the top are representative of the beam size and location (red) relative to the cavity (black) at the indicated locations (vertical lines); the cavity center has been indicated with a cross, and the inner and outer circles indicate the inner and outer surfaces of the cavity wall. Beam horizontal and vertical sizes are correctly scaled to the cavity size, and correspond with the data shown in Fig. 1. With the exception of one anomalous data point at 84 cm, the peak of each curve occurs between the distance at which the beam edge just overlaps the cavity center and the distance at which the beam just fills the cavity interior.

less on the choice of beam axis placement relative to the cavity center, and so the curves in Figs. 4 and 6 for on-axis (a) and off-axis (c and d) cases tend to converge at large distances from the beam window.

The more rapid radial expansion of the beam from the S-band linac compared to the beam from the L-band linac in this testing also helps explain why the signals measured in the S-band cases change faster with increasing distance from the beam window than those in the L-band cases.

Two datasets were taken for the off-axis configuration because one corresponds to a shift of the beam axis towards the pickup loop (d), while one corresponds to a shift of the beam axis away from the pickup loop (c). This produces an asymmetry in the cavity response which is maximized when the beam is small compared to the cavity and disappears when the beam radius is larger than the cavity diameter. Since both resonant drive and non-resonant drive interactions are at play here, this influences the relative strengths of the fields detected in these cases. In general, when the cavity offset moves the beam axis towards the $\dot{B}$ loop, this decreases the distance from the loop to the centroid of that portion of the beam passing through the cavity, and therefore would be expected to increase the detected signal [curve (d) having higher values than curve (c)]. This is evident in three of the cases plotted in Fig. 4. However, in the S-band, high-Q case, this is reversed, and curve (d) has lower values than curve (c). In this case, the interaction is strongly resonant, so that a significant fraction of the azimuthal magnetic field detected by the loop should be due to the cavity mode. In this case,

the cavity fields and the beam fields are both important, but are out of phase.

In contrast to the S-band linac data, the L-band linac data shows a significantly larger amount of structure. There are a number of possible factors contributing to this. First, there is increased shot-to-shot variation in the beam from the L-band linac; this is a key reason why the data in these figures has been normalized to the beam current, with that normalization on the L-band linac relying on identifying corresponding points in the envelope modulation detected on the linac's Bergoz ICT current monitor and on the cavity signal. This introduces both the possibility of differences in the signal value and errors or ambiguities in matching the corresponding points on the beam current and cavity signal waveforms, which could introduce error. A minimum of three shots were therefore taken at each combination of independent variable values to try to reduce the impact of these errors. Additionally, there was more opportunity for scattered radiation to affect the cavity response in these tests. In particular, there were indications of effects from radiation backscattered from a lead shield wall located 216 cm downstream from the beam window on the L-band linac [visible in the background of Fig. 7(b)]. In the low-Q test conducted on the L-band linac, the cavity backplane was removed to spoil the cavity Q; the front plate was left in place to keep the scattering and beam interception occurring on the upstream side of the cavity constant. For cavity locations of about 1.4 m or larger in this case, the cavity signal detected in all the 0° cases [on-axis (a) and off-axis (c and d)] increased noticeably. In these three cases, the cavity was oriented such that there was a direct line of sight from the lead wall into the cavity interior, and therefore to the pickup loop. In the 90° case (b), where the cavity interior was oriented away from both the beam window and the lead wall, this sudden increase of signal was not seen. That increase is therefore likely the result of low energy backscattered radiation, which would not be able to pass through the 1/8″ thick aluminum backplane (e.g., electrons with energies below about 1.4 MeV), directly impinging upon the $\dot{B}$ loop.

B. Waveguides

1. S-band waveguide

The S-band waveguide was placed with its interaction region center aligned to the beam axis, with its upstream flange edge initially located 21 cm downstream of the Ti foil window [Fig. 7(a)]. The interaction region had been tuned to provide a broad resonance at 2856 MHz, which was 10s of MHz wide. Several orientations, distances, and offsets were then tested, as shown in Fig. 7(c). At the nominal location, a waveguide power of 30.8 dBm was detected. Adjusting the waveguide horizontally in the direction perpendicular to the beam axis generally reduced the waveguide power as shown with the black circles in the figure. The asymmetry is due to the nearby presence of the waveguide end. With the waveguide center aligned with the beam axis, additional measurements were taken with the waveguide rotated 90° [Fig. 7(b)], so that the beam was striking the narrow side of the waveguide (indicated by squares in the figure). Measurements
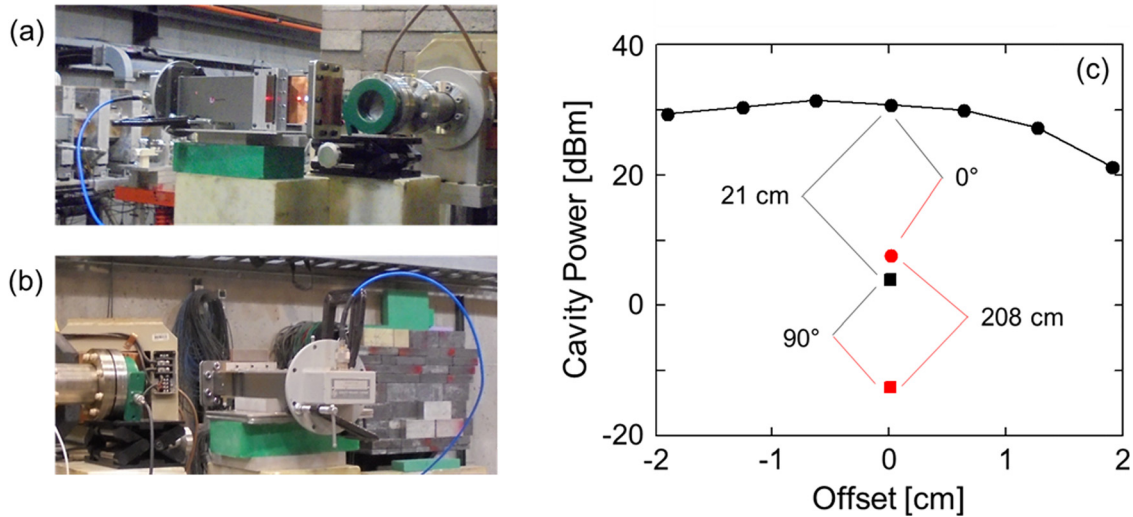
FIG. 7. S-band waveguide testing on the S-band linac: (a) standard orientation, (b) 90° orientation, (c) cavity power as a function of offset for standard orientation (circles) and 90° orientation (squares) at distances of 21 cm (black) and 208 cm (red) downstream from the beam window.

were also taken at a distance of 208 cm downstream from the beam window (indicated by red marks in the figure). As expected, both of these changes reduced the power in the waveguide, but again showed that power deposited is detectable over a wide range of non-ideal conditions.

2. L-band waveguide

The L-band waveguide was similarly tested on both the S-band and L-band linacs. In testing the S-band linac, the waveguide outer wall (not the end flange) was located 41 cm downstream from the beam window. With the waveguide in a normal orientation [long side of the waveguide facing the beam window, similar to Fig. 7(a)], the waveguide power was 22.6 dBm (266 dBm/A) with the beam axis aligned to strike 10.2 cm from the waveguide end (the optimal drive point for the L-band) and 23.7 dBm (279 dBm/A) with the beam axis aligned to strike 3.8 cm from the waveguide end (the optimal drive point for the S-band). With the waveguide rotated to the 90° orientation [similar to Fig. 7(b)], the

waveguide power was now 17.6 dBm (207 dBm/A) with the beam aligned to 10.2 cm and 21.0 dBm (247 dBm/A) with the beam aligned to 3.8 cm.

Figure 8 shows typical examples of the beam current (black) and the crystal detector signal (red) measured with the L-band waveguide tested on the L-band linac. The beam envelope modulation is clearly apparent, and that modulation is very well replicated in the RF envelope detected by the crystal. In this case, the waveguide was located 21 cm downstream from the beam window in the normal orientation and 22 cm downstream from the beam window in the rotated orientation, measured to the waveguide outer wall (not the end flange), and was aligned to place the beam at the center of the interaction region, 10.2 cm down from the waveguide end (the optimal location for driving L-band signals). The left panel shows the standard configuration, with the wide side of the waveguide facing the beam, while the right panel shows the rotated configuration, with the narrow side of the waveguide facing the beam. In the former case, the peak waveguide power is 37.1 dBm (5.16 W) and the corresponding
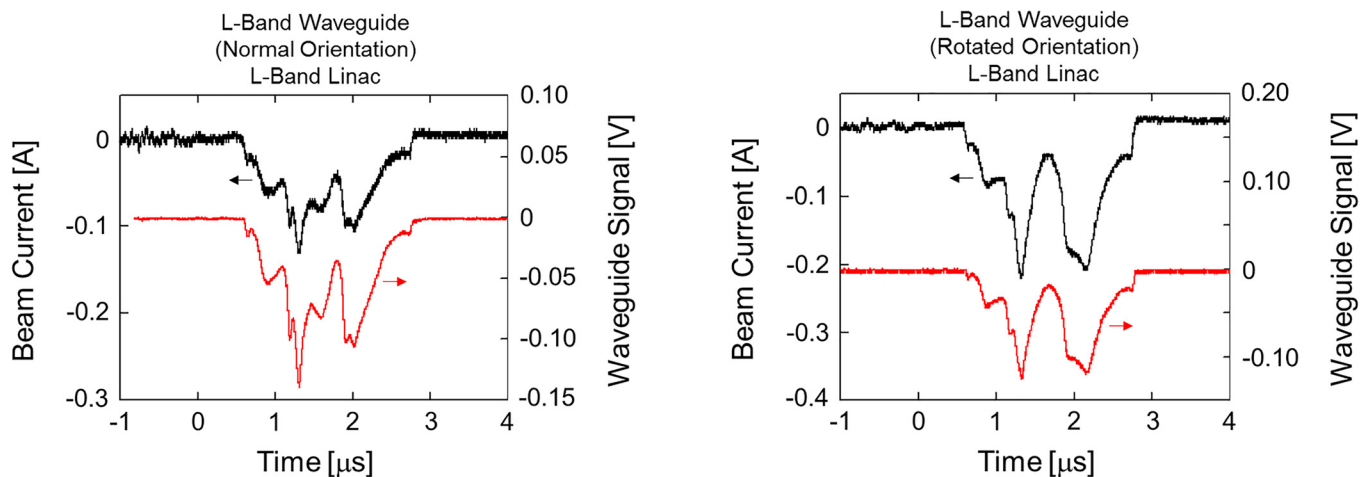

FIG. 8. Beam current (black, left scale) and waveguide signal (red, right scale) measured with the L-band waveguide and the L-band linac in the standard (left panel) and rotated (right panel) orientations.
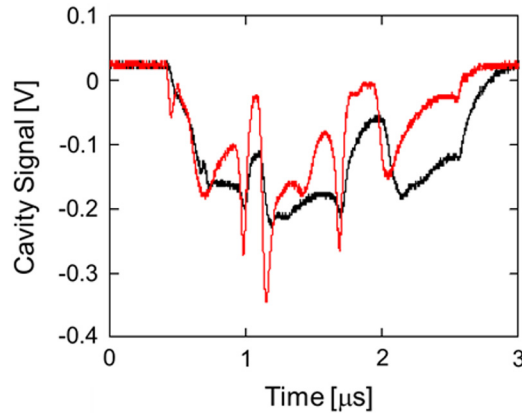
FIG. 9. Typical L-band cavity signals during testing on the L-band linac, with the cavity in 0° on-axis (black) and 90° (red) configurations.

peak beam current is 132 mA (for 281 dBm/A), while in the latter case the peak waveguide power is 36.5 dBm (4.42 W) and the corresponding peak beam current is 220 mA (for 166 dBm/A).

C. L-band cavity

Figure 9 shows typical data taken from testing the L-band cavity on the L-band machine, in both the 0° on-axis (black) and 90° (red) orientations, with the cavity 21 cm from the beam window. The beam current in these cases was 176 mA for the 0° orientation and 84 mA for the 90° orientation. The beam current envelope modulation shapes were almost identical in the two cases, although the current amplitudes were different. Note the cavity signal detected at the crystal decays much faster in the 90° orientation rather than the 0° orientation. This underlines the fact that in the 0° orientation, we are driving cavity modes, due to the cavity tuning and relatively high Q, while in the 90° case, the cavity is just sensing the beam passage.

IV. BEAM TRANSPORT THROUGH METAL

A. S-band cavity

The maximum distance downstream from the windows available on the two linacs was very limited. In order to produce a more challenging transport environment, aluminum and stainless steel plates were placed between the beam window and the cavity, as shown in Fig. 10. Two configurations were used. The first, labeled "A" in Fig. 10, used aluminum

or stainless steel plates placed just downstream from the window (and in the S-band linac, the Pearson coil), while the second, labeled "B" in Fig. 10, used stainless steel plates attached to the front face of the cavity. The S-band cavity was used for all of these tests, and was placed 21 cm downstream from the window in each case. The aluminum and stainless steel plates fully obscured the cavity from the line of sight to the window in configuration A, and while they did not fully block the line of sight to the window in configuration B, they did block the beam, as verified by glass plate exposures taken just upstream of the cavity. Configuration B was only performed on the S-band linac. Additionally, an off-axis test series with configuration A was performed on the S-band linac. The relative sizes and locations of the on-axis beam, the off-axis beam, and the stainless steel plates with the S-band cavity are shown in Fig. 11. Note that the on-axis beam in this case, while overlapping the cavity center, was high by about 9% of the cavity radius. Alignment of the L-band beam axis with the cavity center was performed using the alignment laser as discussed earlier. In each case, metal was added in 1/8″ (3.2 mm) increments.

The results of these tests are shown in Fig. 12. As in Fig. 4, this figure consists of four panels. The top row presents the data taken on the S-band linac, while the bottom row presents the data taken on the L-band linac. The left column shows data taken with the S-band cavity in a low-Q state, while the right column shows data taken with the cavity in a high-Q state. In each panel, the vertical axis again represents the normalized cavity power in dBm/A, representing the RF power detected by the crystal divided by the beam current. The horizontal axis represents the thickness of metal used. As before, a single data point was taken for each value of metal thickness in the case of the S-band linac, and the nominal current of 85 mA was used for normalization, while a minimum of three shots per value of metal thickness was taken in the case of the L-band linac, and the signal amplitude and normalization currents were taken from the corresponding locations on the respective waveforms. Red curves present the data for aluminum, black curves present the data for stainless steel, and dashed lines present the data for the off-axis case. The data for configuration B with stainless steel is indicated on the plots with blue lines. Additionally, vertical dotted lines indicate the electron range in aluminum (red) and iron (black), for 20 MeV (top row) and 25 MeV (bottom row) electrons, as computed by the NIST ESTAR database[34] using the Continuous Slowing-Down Approximation (CSDA), using
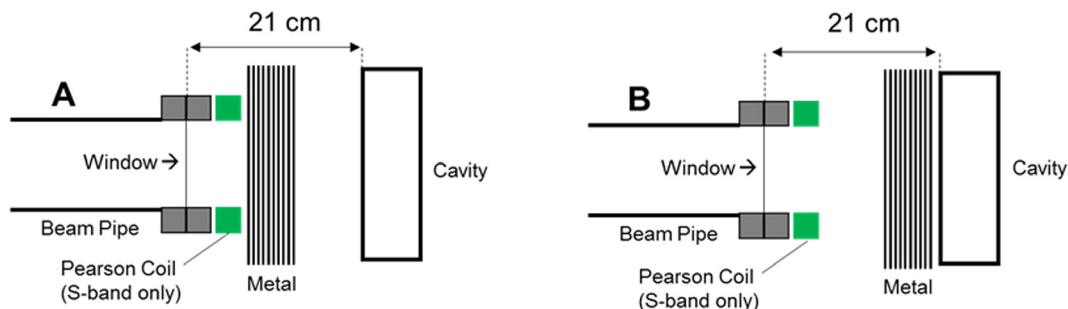

FIG. 10. Two test configurations used for studies of beam propagation through metal.
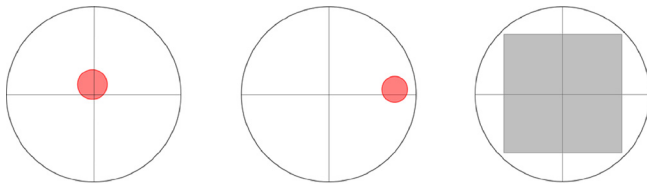
FIG. 11. Relative sizes and orientations for cavity (black circle with cross), S-band beam spot (red), and stainless steel plates (gray) in the on-axis (left), the off-axis (center), and configuration B tests (right) described in Sec. IV. Beam spots were determined from the exposure of glass plates placed immediately upstream of the cavity.

iron as a proxy for steel and assuming a density of $8 \, \text{g/cm}^3$ (see Appendix).

As before, general trends can be observed from comparison of these datasets. First, we again see that signals detected at the crystal are higher when the cavity Q is higher, and when the cavity is tuned to the beam modulation. In particular, going from a low Q to a high Q condition with configuration A on the S-band linac allowed a detectable cavity signal to be observed through approximately an extra 1.5 cm of Al and approximately an extra 0.3 cm of steel. However, we again find that, even when the cavity Q is spoiled by removing its backplane and the cavity is not tuned to the beam, the beam still induced a signal which could be detected after

traveling through over 5 cm of Al and almost 2 cm of steel on the L-band linac.

As expected, for a given test configuration (i.e., configuration A on-axis, configuration A off-axis), detectable signals could be produced through thicker regions of Al than steel. The CSDA ranges, mentioned above, provide an estimate for the depth of penetration of a single electron in a given material. For 20 MeV electrons, these ranges are 3.91 cm for Al and 1.29 cm for Fe, while for 25 MeV electrons, they are 4.67 cm for Al and 1.51 cm for Fe. In our testing, detectable signals were observed at thicknesses greater than the calculated CSDA range, suggesting a transition from electron beam driving of the cavity to x-ray driving of the cavity. Although x-ray photons will not directly drive fields or currents in the cavity, they can generate secondary electrons within the cavity which can drive these fields and currents. Approaching the CSDA range also seems to affect the slope of the curves in many cases, often with an increasing negative slope near the CSDA range followed by a reduction in the slope past the CSDA range, again presumably due to a loss of electrons from the beam and their replacement with more-penetrating but more weakly interacting x-rays. This will be seen more clearly in the L-band cavity data presented next.

Configuration B also exhibits a much higher signal than the other cases using steel and, in fact, a higher signal than
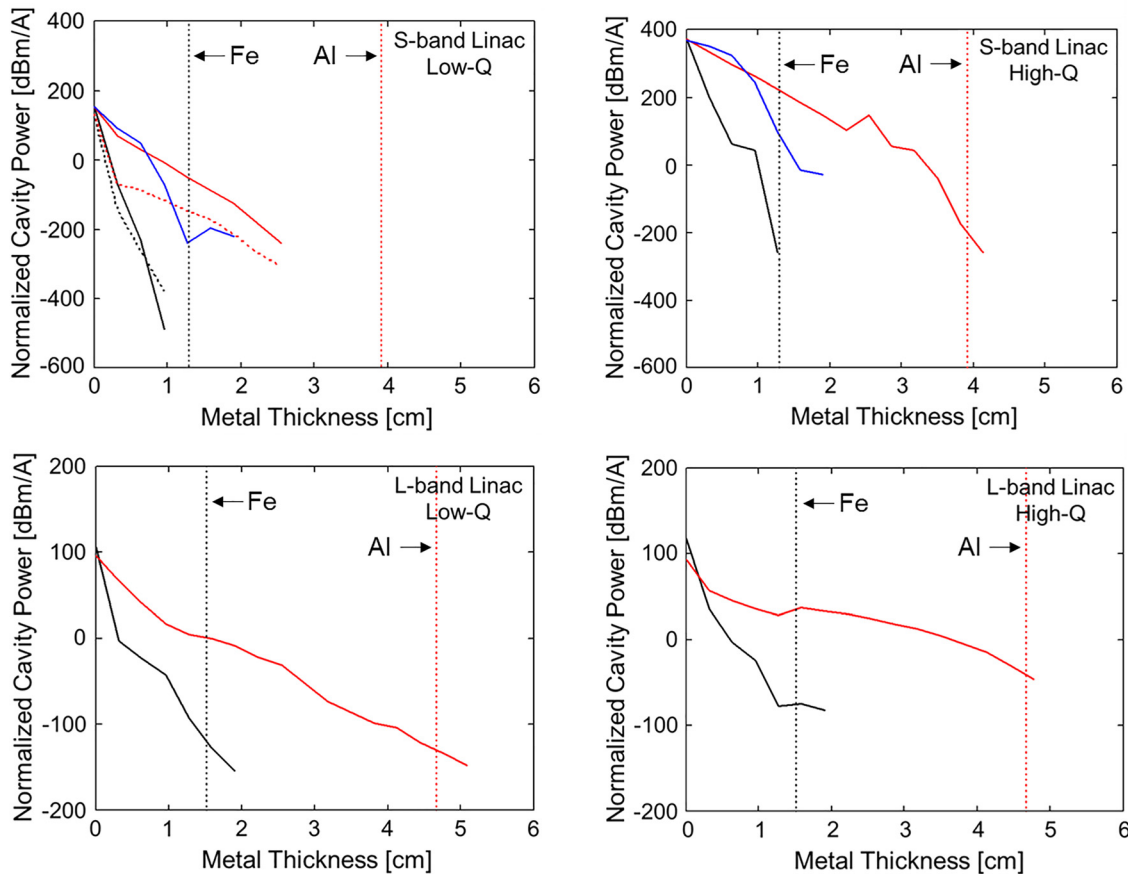

FIG. 12. Normalized cavity power detected from the S-band cavity on the S-band linac (top row) and the L-band linac (bottom row) under low-Q (left column) and high-Q (right column) conditions. Configuration A results for aluminum are shown with red lines, while configuration A results for stainless steel are shown with black lines; solid lines indicate on-axis tests, while dashed lines represent off-axis tests. The blue line represents measurements with stainless steel in configuration B. The vertical dotted lines represent the CSDA range of electrons in iron (black) and aluminum (red) for 20 MeV (top row) and 25 MeV (bottom row) electrons.

the configuration A tests with Al for thicknesses less than about 1 cm. This is presumably because in configuration A tests, the air gap between the metal sheets and the cavity face would enable a significant fraction of the secondary radiation to escape to the sides, so that it is lost from the system, and does not contribute to current inside the cavity.

Finally, we consider the offset cases shown with dashed lines in the top left panel of Fig. 12. In this case, the arrangement was still configuration A, with an air gap between the metal and the cavity, but the cavity was offset somewhat to one side. The cavity offset was much less than that used in the air propagation tests described earlier, and so the reduction in induced signal strength with no metal present was negligible. The offset test described here is different from all the other tests, in that the effect of small amounts of metal was identical for Al and steel, while the effect of additional amounts of metal was not. In particular, the off-axis and on-axis configuration A tests with steel were essentially identical. This is reasonable, as glass plate images of the beam with a single 1/8″ layer of steel show that the scattering of the beam is so large that the beam radius striking the cavity is much larger than the cavity offset relative to the beam axis, and therefore no change in cavity response would be expected from such a small change in incident beam location.

B. L-band cavity

The L-band cavity in a high-Q mode was also tested on the L-band linac with varying degrees of metal installed just downstream of the beam window (i.e., configuration A), and with the cavity itself located 21 cm from the window. The results are shown in Fig. 13. As before, the vertical scale is presented as normalized cavity power, i.e., RF power detected at the crystal detector at the peak of the cavity
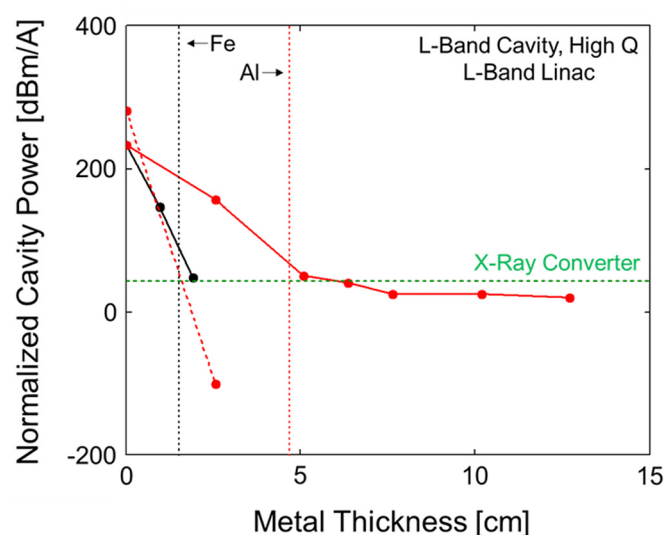

FIG. 13. Normalized cavity power as a function of metal thickness for the L-band cavity, tested in high-Q mode on the L-band linac, with the metal placed in Configuration A. Results with aluminum plates with the cavity in 0° (solid red) and 90° (dashed red) orientations, stainless steel plates with the cavity in 0° orientation (black) and an x-ray converter with the cavity in 0° orientation (green dashed) are shown. Vertical dotted lines are the CSDA ranges for 25 MeV electrons in iron (black) and aluminum (red).

signal waveform divided by the beam current at the corresponding point in its own waveform. Individual data points are indicated here due to the relative sparseness of the data compared to that presented elsewhere. The effect of stainless steel on the cavity in standard, 0° configuration [as in Fig. 3(a)] is shown with the black solid line, and the CSDA range for 25 MeV electrons in iron is shown with the vertical black dotted line. The effect of aluminum on the cavity in the standard configuration is shown with the red solid line, the effect of aluminum on the cavity in the 90° configuration [as in Fig. 3(b)] is shown with the red dashed line, and the CSDA range for 25 MeV electrons in aluminum is shown with the vertical red dotted line. Additionally, the cavity response with the x-ray converter installed and the cavity in the 0° configuration is shown with the horizontal green dashed line.

The general response is similar to that of the S-band cavity. Steel provides a greater reduction in the cavity signal per unit thickness than aluminum, consistent with its shorter CSDA range. The 90° orientation generally responds more poorly to additional metal upstream due to its inability to enable the drive of the cavity fundamental resonant mode. In this case, the performance is enhanced due to the orientation of the cavity during testing, with the pickup loop located on the downstream side of the cavity, along the beam axis, which would facilitate direct striking of the loop by both secondaries and the primary beam passing through the thin cavity walls. This explains why the 90° signal is higher than the 0° signal for metal thicknesses of zero. For the cavity in the 0° configuration, addition of aluminum reduces the induced signal, with the slope steepening near the CSDA range of electrons in the aluminum. For metal thicknesses much larger than the CSDA electron range, the beam hitting the cavity is assumed to consist largely of x-rays. This is consistent with the fact that the signal for such thicknesses of aluminum is very similar to that produced using the x-ray converter (consisting of 2.54 mm of tungsten and 48.3 mm of aluminum) in lieu of the aluminum plates, which should perform slightly better than stacks of aluminum plates as it was actually optimized for this purpose. Once the primary electron beam is fully converted to x-rays, the attenuation produced by additional layers of aluminum is much reduced, and the normalized cavity power curve flattens. At this point, interaction with the cavity is presumed to be through the generation of secondary electrons produced inside the cavity by the x-rays themselves. Combining the observation of increased performance in the 0° orientation compared to the 90° orientation, suggesting that the cavity is being driven resonantly in the former case, and the flattening of the response curve near the expected level for a pure x-ray drive, suggesting that at thicknesses above about 7 cm, the cavity is being driven almost entirely by x-rays, implies that at least some of the L-band frequency content in the electron beam survives the conversion into x-rays, and again survives the conversion into photoelectrons in the cavity.

C. L-band waveguide

Figure 14 shows the response of the L-band waveguide on the L-band linac with the x-ray converter target installed.
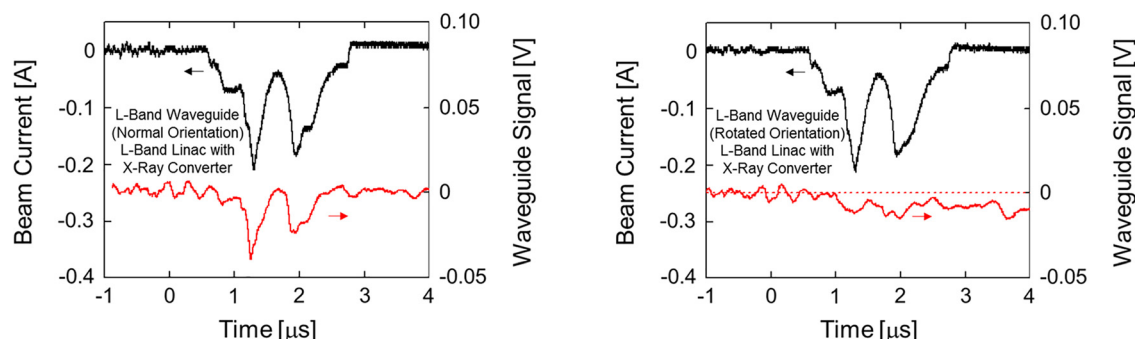
FIG. 14. L-band waveguide response (red) and L-band linac electron beam current (black), for the waveguide in 0° (left) and 90° (right) orientations, with the x-ray converter installed.

The waveguide was located 22 cm downstream from the window (measured to the front face of the waveguide outer wall), and was tested in both normal orientation [longer side towards beam, as in Fig. 7(a)] and rotated orientation [shorter side towards beam, as in Fig. 7(b)]. The waveguide was again aligned with its interaction region center along the nominal beam axis; this interaction region center is located 10.2 cm from the waveguide end, and is the optimal drive point for the L-band. Figure 14 shows the electron beam current (black), again exhibiting its enhanced current envelope modulation, as well as the crystal detector output signal (red), with the normal orientation result in the left panel and the rotated orientation result in the right panel. An additional dotted line is added to the crystal signal in the latter case to more clearly define zero. In the former case, the peak waveguide power is −6.78 dBm (0.21 mW) with a corresponding peak current of 210 mA, while in the latter case, the peak waveguide power (in the first of the two signal spikes) is −14.5 dBm (35.9 μW) with a corresponding peak current of 213 mA. For a well-designed x-ray converter with a 25 MeV electron beam, typically 30%–40% of the electron beam energy will be converted into x-rays. Naively taking 35% of the waveguide power measured without the x-ray converter would predict 1.8 W in the normal orientation and 1.5 W in the rotated orientation for the power produced using the x-ray converter. Clearly the actual power induced is much lower.

V. DISCUSSION

The objective of this project was to investigate the impact of propagation through matter on a beam's longitudinal properties, and how this, in turn, affects its ability to interact with RF structures which are both in-band and out-of-band with respect to the beam modulation. Such longitudinal properties exist on at least two length scales in RF linacs: modulation of the beam into microbunches spaced at the RF period and modulation of the beam on a longer time scale, for example, due to gating on and off of the beam or changes in the cathode control grid voltage. To investigate the impact of modulation at the RF frequency, we used S-band and L-band structures on both S-band and L-band accelerators. To investigate the impact of modulation on slower time scales, we used the L-band accelerator in a mode where a significant longitudinal structure is produced

on a time scale of roughly 100 ns. Relatively short propagation distances in air were available at IAC. To simulate longer distances, shielding materials of varying thickness were used, although this does not properly simulate all atmospheric effects.

Our data clearly show that interaction of a modulated beam and an RF structure does not require a resonant interaction between the beam and the cavity, although such resonant condition definitely maximizes the cavity response, and that differences exist between interactions based on the primary electron beam, and interactions based on photoelectrons produced inside the structures by x-rays. This data also suggests that the RF modulation of the beam is not fully washed out as it propagates through air or metal, and that some of that modulation is retained even through the process of conversion from primary electrons to x-rays and then to photoelectrons inside the RF structures.

There are at least three classes of interaction playing a role in this experiment. First, the beam charge (or x-ray induced photoelectrons) can drive RF cavity modes in resonant structures. This requires that the structure be resonant at a frequency which is present in the beam, and that the beam drives the resonant structure at the correct location (i.e., the axis of a cavity). If the beam is not placed properly, or if the structure is not resonant at a frequency present in the beam, this effect will be negligible. However, when these conditions are met, the response can be very strong. For example, the ability of the L-band linac to drive the L-band cavity through significant layers of metal seems likely to be a result of a resonant drive of the relatively high-Q cavity, allowing whatever L-band frequency content that survived the conversion from primary electrons into x-rays and then into photoelectrons to still drive cavity fields. Second, the passage of the electron beam (or x-ray induced photoelectrons) through the structure can introduce transient fields which can couple out of the structure, even though no strong resonant mode is driven. This effect is generally weaker than the resonant drive, but is more robust, as it does not require the structure to be resonant, and is much weaker when the incident beam consists entirely of x-rays (for example, compare Figs. 8 and 14). However, it does not require the structure to be resonant, does not require the beam to have specific frequency content, and does not require a specific orientation of the structure. Third, net charge interception or loss can occur. This

appeared to be only a minor effect in the testing described here, as the beam energies were relatively high and the RF structures consisted of relatively thin metal components, minimizing the capture of primary beam electrons. Like a non-resonant beam drive, charge interception does not require a structure to be resonant, and does not require the beam to have particular frequency content. However, there must be sufficient mass in the structure or around the structure to enable this process to occur. If this is not the case, the efficiency of charge collection will be low.

ACKNOWLEDGMENTS

APPENDIX: MODELS FOR BEAM INTERACTIONS

1. Stopping power and CSDA range relations

Graphs of the stopping power (dE/dx) and the Continuous Slowing Down Approximation (CSDA) range for electrons in aluminum and iron (steel), generated from the NIST ESTAR site,[34] are presented in Figs. 15 and 16. A decent approximation for the stopping power in both materials is given by

$$dE/dx = \left(2\,\text{MeV-cm}^2/\text{g}\right)\rho\left(\text{g/cm}^3\right), \quad (A1)$$

where ρ is the material density (2.7 g/cm^3 for Al and 7.7 g/cm^3 for steel). Thus, the kinetic energy (in MeV) of electrons emerging from an absorber of thickness x (in inches) is roughly given by

$$E = E_o - 13.7\,x(\text{in}) \quad \text{Al} \quad (A2)$$

and

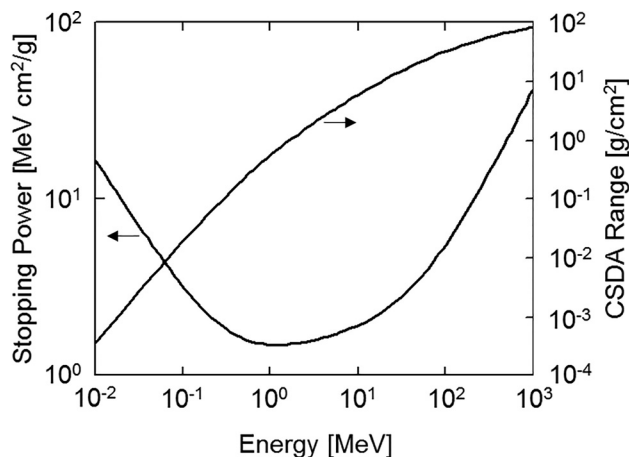$$E = E_o - 39.1\,x(\text{in}) \quad \text{Steel}, \quad (A3)$$

FIG. 15. Electron stopping power and CSDA range in aluminum (from Ref. 33).
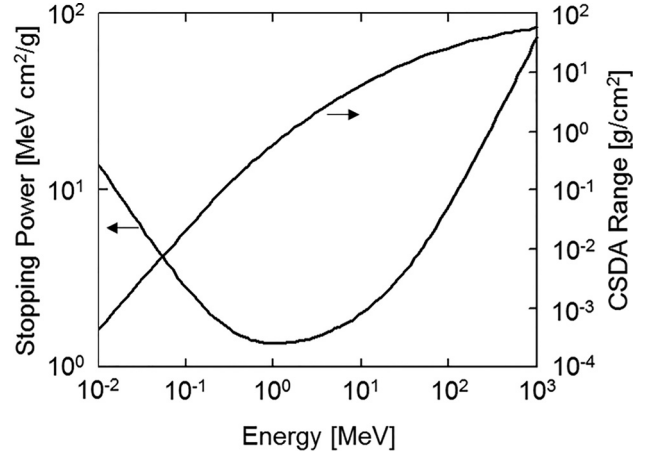

FIG. 16. Electron stopping power and CSDA range in iron (steel) (from Ref. 34).

where E_o is the electrons' initial energy. As an example, the range of a 20 MeV electron in aluminum is about 1.5 in. and about 0.5 in. in steel.

2. Electron scattering

An electron collision with a massive nucleus will not result in significant energy transfer, but will alter the electron trajectory (and can give rise to bremsstrahlung). While the most probable value of the average scattering angle is zero, it is possible to obtain a relation for the average mean square scattering angle $\langle \theta^2 \rangle$. Performing this calculation gives an expression of the form $\langle \theta^2 \rangle = aNx(Z/E)^2$, where a is a constant, N is the atomic number density of the scattering medium, Z is the atomic number, x is the distance into the medium, and E is the electron kinetic energy. A useful empirical expression for titanium is

$$\langle \theta^2 \rangle = 80\,x(\text{cm})/E^2, \quad (A4)$$

with E in MeV. For a 1-mil titanium window (used on both IAC accelerators), the RMS angle for 20-MeV electrons is 2.25×10^{-2} rad. Thus, a thin pencil beam would have a diameter of ∼4.5 cm after propagating 1 m in a vacuum.

Approximate scattering relations for other materials are given in the following equations:

$$\langle \theta^2 \rangle = 30\,x(\text{cm})/E^2 \quad \text{Al}, \quad (A5)$$

$$\langle \theta^2 \rangle = 140\,x(\text{cm})/E^2 \quad \text{Fe (steel)}, \quad (A6)$$

$$\langle \theta^2 \rangle = 60\,x(\text{m})/E^2 \quad \text{air}. \quad (A7)$$

Very roughly, 0.5 in of aluminum, 0.125 in of steel, and 100 cm of air give the same RMS scattering angle (∼0.33 rad). For the metals, the beam diameter would expand to ∼8 in after propagating a distance of 12 in.

3. Characteristic behavior of a resonant cavity

For a microwave cavity oscillating in a single mode, the simplest model for describing the behavior is a parallel RLC circuit driven by a current source. The driving current

produces a voltage across the parallel combination of inductance, capacitance, and shunt impedance that can be identified as the product of the peak electric field E_o on the cavity axis multiplied by the width between cavity endplates d. The resonant frequency is given by $\omega_o = 2\pi f_o = (LC)^{-1/2}$ and the width of the resonance (-3 dB points) is $\Delta f = f_o/Q$, where Q is the quality factor equal to $\omega_o RC$. The voltage produced in the cavity scales linearly with the shunt impedance R (i.e., a less lossy cavity—higher Q—produces a higher voltage). The characteristic cavity fill (decay) time is given by $\tau = Q/\pi f_0$.

Using the network analyzer, we measured resonant frequencies of the S-band and L-band cavities under a variety of conditions. The inferred quality factors ranged from about 220 for the S-band cavity to a high of 930 for the L-band cavity, and could be varied somewhat by loosening or tightening fasteners. For the S-band cavity tuned to the linac resonance, the calculated time constant was only 77 ns, which was too short to be clearly observed. However, for the L-band cavity, the calculated time constant increased to ~715 ns, and it was clearly observed at the termination of the microwave power pulse (Fig. 9).

4. Bremsstrahlung production and X-ray attenuation

For an optimized thick-target high-Z x-ray converter, the efficiency of converting electron kinetic energy into x-ray energy varies as $\eta = E/60$, with E in MeV, and the on-axis dose rate at one meter from the converter is approximately given by

$$dD/dt\,(R/s) = 1.1 \times 10^3 E^{2.8} I, \qquad (A8)$$

where I is the beam current. Such a converter usually consists of a one-third range layer of tantalum or tungsten ($Z \sim 73$), backed by a low-Z material such as aluminum of sufficient thickness to completely stop the primary electrons. If the high-Z layer is replaced by a lower-Z material, the dose rate will be decreased roughly by the square root of the atomic number ratio (Z/73), and if an additional material is used, the x-rays will be further attenuated by the factor $\exp(-\mu\rho x)$, where $\mu = 0.03$ cm^2/g is the x-ray attenuation coefficient. As an example, for an absorber of 5 in of aluminum, the range of a 20 MeV electron is ~4 cm, which would give an estimated dose rate at one meter of 2 MR/(s-amp). The additional aluminum would further decrease the dose rate by a factor of about 2, to 1 MR/(s-amp).

[1]T. A. Edison, U.S. patent 307,031 (21 October 1884).
[2]P. Zhang, A. Valfells, L. K. Ang, J. W. Luginsland, and Y. Y. Lau, Appl. Phys. Rev. **4**, 011304 (2017).
[3]C. A. Brau, *Free-Electron Lasers* (Academic Press, 1990).
[4]*High-Power Microwave Sources and Technologies*, edited by R. J. Barker and E. Schamiloglu (IEEE Press, New York, 2001).
[5]J. R. Harris and P. G. O'Shea, IEEE Trans. Electron Devices **53**, 2824–2829 (2006).
[6]J. G. Neumann, J. R. Harris, B. Quinn, and P. G. O'Shea, Rev. Sci. Instrum. **76**, 033303 (2005).
[7]K. R. Spangenberg, *Vacuum Tubes* (McGraw-Hill, New York, 1948).
[8]C. A. Spindt, C. E. Holland, A. Rosengreen, and I. Brodie, IEEE Trans. Electron Devices **38**, 2355 (1991).
[9]A. Pedersen, A. Manolescu, and A. Valfells, Phys. Rev. Lett. **104**, 175002 (2010).
[10]K. L. Jensen, D. A. Shiffler, I. M. Rittersdorf, J. L. Lebowitz, J. R. Harris, Y. Y. Lau, J. J. Petillo, W. Tang, and J. W. Luginsland, J. Appl. Phys. **117**, 194902 (2015).
[11]M. Reiser, *Theory and Design of Charged Particle Beams* (Wiley, New York, 1994).
[12]A. Faltens, E. P. Lee, and S. S. Rosenblum, J. Appl. Phys. **61**, 5219 (1987).
[13]B. R. Poole and J. R. Harris, Phys. Plasmas **20**, 043108 (2013).
[14]A. Gover, Phys. Rev. Spec. Top. - Accel. Beams **8**, 030701 (2005).
[15]J. R. Harris, J. G. Neumann, K. Tian, and P. G. O'Shea, Phys. Rev. E **76**, 026402 (2007).
[16]Y. C. Mo, R. A. Kishek, D. Feldman, I. Haber, B. Beaudoin, P. G. O'Shea, and J. C. T. Thangaraj, Phys. Rev. Lett. **110**, 084802 (2013).
[17]B. R. Poole, D. T. Blackfield, Y.-J. Chen, J. R. Harris, and P. G. O'Shea, "Space charge waves in mismatched beams," in *Proceedings of the 2009 Particle Accelerator Conference, Vancouver, Canada, 4–8 May 2009*.
[18]J. R. Harris and P. G. O'Shea, Phys. Plasmas **15**, 123106 (2008).
[19]J. R. Harris and J. W. Lewellen, J. Appl. Phys. **108**, 083301 (2010).
[20]J. R. Harris, J. W. Lewellen, and B. R. Poole, J. Appl. Phys. **114**, 063304 (2013).
[21]J. R. Harris, J. W. Lewellen, and B. R. Poole, J. Appl. Phys. **116**, 133302 (2014).
[22]J. R. Harris, B. R. Poole, and J. W. Lewellen, J. Appl. Phys. **122**, 093302 (2017).
[23]R. B. Miller, *An Introduction to the Physics of Intense Charged Particle Beams* (Plenum Press, New York, 1982).
[24]N. Wells, see https://www.rand.org/content/dam/rand/pubs/reports/2006/R3463.pdf for "Soviet Research on the Transport of Intense Relativistic Electron Beams through High-Pressure Air," RAND Corporation Report R-3463-DARPA, (1987).
[25]R. B. Miller, U.S. patent 5,608,403 (1997).
[26]K. C. Gendreau, Z. Arzoumanian, S. J. Kenyon, and N. S. Spartana, U.S. patent 9,117,622 (2015).
[27]J. Mitchell, "Pulsar navigation & X-ray communication demonstrations with the NICER payload on ISS," in *1st Annual ISS R&D Conference, Denver, CO, 25–28 June 2012*.
[28]L. M. B. Winternitz, K. C. Gendreau, M. A. Hassouneh, J. W. Mitchell, W. H. Fong, W.-T. Lee, F. Gavriil, and Z. Arzoumanian, "The role of X-rays in future space navigation and communication," in *36th Annual AAS Guidance and Control Conference, Breckenridge, CO, 1–6 February 2013*.
[29]S. Shi-Bin, X. Lu-Ping, Z. Hua, and G. Na, Chin. Phys. B **24**, 094215 (2015).
[30]S. Li-zhi, Z. Bao-sheng, and L. Yong-an, Proc. SPIE **9207**, 920716 (2014).
[31]H. Li, X. Tang, S. Hang, Y. Liu, and D. Chen, J. Appl. Phys. **121**, 123101 (2017).
[32]J. R. Harris, J. G. Neumann, and P. G. O'Shea, "Modulation of intense beams in the University of Maryland Electron Ring," in *Proceedings of the 2005 Free-Electron Laser Conference, Stanford, CA, 21–26 August 2005*.
[33]See iac.isu.edu for more information.
[34]See https://physics.nist.gov/PhysRefData/Star/Text/ESTAR.html for more information.